J|A|C|S ARTICLES

Published on Web 12/03/2009

Mechanism of Water Splitting and Oxygen−Oxygen Bond Formation by a Mononuclear Ruthenium Complex

Xinzheng Yang and Michael B. Hall*

Department of Chemistry, Texas A&M University, College Station, Texas 77843-3255

Received May 20, 2009; E-mail: mbhall@tamu.edu

Abstract: Density functional theory (DFT) predicts a detailed mechanism for the reported potential photocatalytic system for solar hydrogen production from water, (P-da-PNN)RuH(CO) (**1**, P-da = dearomatized at the phosphorus side arm, PNN = (2-(di-*tert*-butylphosphinomethyl)-6-diethylaminomethyl)pyridine) (*Science* **2009**, *324*, 74). In the initial thermal reaction, the coordination of a water molecule is followed by cleavage of an O−H bond and aromatization of the PNN ligand to form (PNN)RuH(CO)(OH) (**3′**), the most stable complex in the reaction. This low-barrier step is followed by the rate-determining dearomatization and formation of H_2. Next, a second water molecule is activated, resulting in the formation of the *cis*-dihydroxo complex (PNN)Ru(CO)$(OH)_2$ (**7**), which photolytically eliminates H_2O_2. Time-dependent DFT calculations predict that the breaking of the two strong Ru−O bonds and the formation of the O−O bond in this photolytic reaction involve low-energy triplet states and singlet–triplet crossings. Rather than regeneration of initial complex **1** after the light-induced H_2O_2 evolution in the catalytic cycle, the DFT calculations predict a new route with a lower energy barrier via the regeneration of **1′**, an isomer of **1** with the unsaturated carbon at the nitrogen side arm of the PNN ligand. This new route involves hydride transfer from the methylene group at the nitrogen side, rather than the previously proposed regeneration of **1** through hydride transfer from the phosphorus side arm of the PNN ligand.

Introduction

The utilization of sunlight as a clean energy source depends on the capture, conversion, and distribution of solar energy. Defects in current photovoltaic devices, such as low conversion efficiency, poor energy density, high cost, and negative environmental impact in their manufacture, have impeded their wide-scale deployment. Thus, the design of efficient artificial photosynthesis systems for harvesting solar energy by production of molecular hydrogen from water as a clean and renewable energy carrier has become one of the foremost challenges in the development of a solar hydrogen economy.[1]

Milstein and co-workers[2] recently reported a potential photocatalytic system in which a monomeric dearomatized ruthenium(II) pincer complex (P-da-PNN)RuH(CO) (**1**, P-da = dearomatized at the phosphorus side arm, PNN = (2-(di-*tert*-butylphosphinomethyl)-6-diethylaminomethyl)pyridine) promoted consecutive thermal H_2 and light-induced O_2 evolution from water. At the beginning of the reaction, the O−H bond of a water molecule was split, H_2 was released slowly at 100 °C, and a second water molecule was activated with the formation of an aromatized *cis*-dihydroxo complex (PNN)Ru(CO)$(OH)_2$ (**7**). Next, O_2 was generated photolytically when **7** was irradiated under 320−420 nm UV−vis light. The presumed light-induced, intramolecular, reductive elimination of H_2O_2, believed to be the source of the O_2 evolution, was shown by isotopic labeling to be an intramolecular O−O bond formation step without the involvement of metal oxo intermediates.[2] Although a footnote in ref 2 reported several density functional theory (DFT) calculations on a transition state for the initial O−H bond cleavage reaction based on a simplified molecular model (*tert*-butyl and ethyl were replaced by methyl), the entire reaction mechanism for the formation of H_2, the splitting of two water molecules, and the regeneration of **1** is still unknown. When this Article was in review, Yoshizawa and co-workers[3] reported a DFT study of the mechanism of thermal H_2 production from water splitting by the model Ru(II) PNN complex (ethyl and *tert*-butyl groups were replaced by methyl). However, the photolytic intramolecular H_2O_2 formation process is absent from their study. In this Article, the thermal processes for a complete reaction cycle with the full ligand structure, detailed transition state, structures and energy profiles for the cleavage of two water molecules, the formation and release of H_2, and the regeneration of catalyst **1** are predicted by DFT calculations. The photolytic intramolecular H_2O_2 formation in **7** is also explored by using the time-dependent (TD) DFT method.

Results and Discussion

Aromatization and Dearomization of the PNN Ligand. To isolate the effect of aromatization and dearomatization of the

(1) (a) Sala, X.; Romero, I.; Rodríguez, M.; Escriche, L.; Llobet, A. *Angew. Chem., Int. Ed.* **2009**, *48*, 2842. (b) Kudo, A.; Miseki, Y. *Chem. Soc. Rev.* **2009**, *38*, 253. (c) Kanan, M. W.; Nocera, D. G. *Science* **2008**, *321*, 1072. (d) Yang, X.; Baik, M. H. *J. Am. Chem. Soc.* **2008**, *130*, 16231. (e) Esswein, A. J.; Nocera, D. G. *Chem. Rev.* **2007**, *107*, 4022. (f) Kodama, T.; Gokon, N. *Chem. Rev.* **2007**, *107*, 4048. (g) Lewis, N. S. *Science* **2007**, *315*, 798. (h) Lewis, N. S.; Nocera, D. G. *Proc. Natl. Acad. Sci. U.S.A.* **2006**, *103*, 15729. (i) Zou, Z.; Ye, J.; Sayama, K.; Arakawa, H. *Nature* **2001**, *414*, 625.

(2) Kohl, S. W.; Weiner, L.; Schwartsburd, L.; Konstantinovski, L.; Shimon, L. J. W.; Ben-David, Y.; Iron, M. A.; Milstein, D. *Science* **2009**, *324*, 74.

(3) Li, J.; Shiota, Y.; Yoshizawa, K. *J. Am. Chem. Soc.* **2009**, *131*, 13548.

10.1021/ja9041065

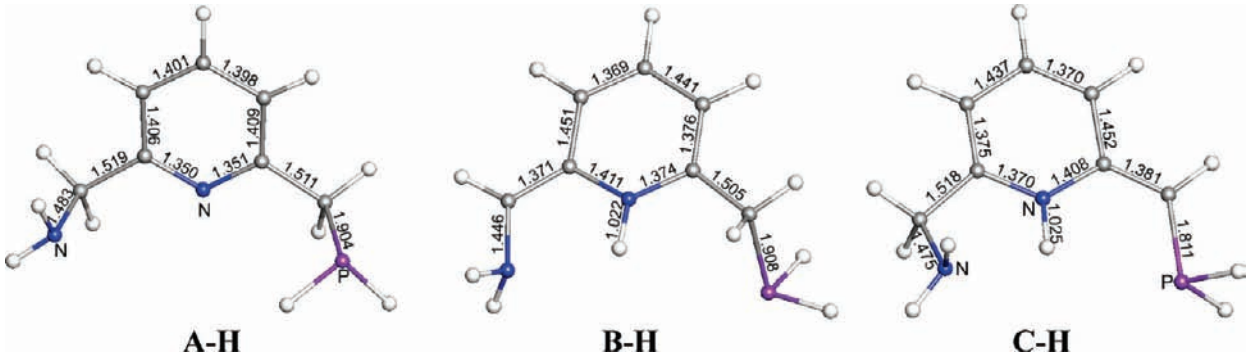

Figure 1. Optimized isomeric PNN-type ligands. Ethyl and *tert*-butyl groups are replaced by H. Bond lengths are in angstroms.

Scheme 1

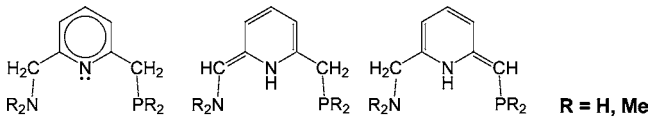

Table 1. Calculated Relative Gas-Phase Electronic Energies (kcal/mol) of the PNN Ligand

structure	A	B	C
R = H	0.00	16.02	12.72
R = Me	0.00	16.42	12.79

central ring in the PNN pincer ligand, three simplified isomeric PNN-type ligands (Scheme 1, here only, ethyl and *tert*-butyl were replaced by H or methyl) were optimized: **A** (PNN), **B** (N-da-PNN), and **C** (P-da-PNN). The optimized structures of **A**−**H**, **B**−**H**, and **C**−**H** are shown in Figure 1. Their relative electronic energies are listed in Table 1.

According to the relative electronic energies listed in Table 1, structure **A** with the aromatized central ring is much more stable than the dearomatized structures **B** and **C**. Comparison of the relative energies of **B** and **C** shows that P-da-PNN is several kcal/mol more stable than N-da-PNN. This is the reason why complex **1**, as synthesized by Milstein and co-workers,[4] is more stable than its isomer **1′** (N-da-PNN)RuH(CO) (see Figure 2 below for more details). These results indicate that the origin of relative stability of the isomers discussed in this Article lies in the aromatization and dearomatization of the PNN ligand.

Complex 1 and Its Isomer 1′. Complex **1**, originally synthesized by Milstein and co-workers[4] for the dehydrogenation of primary alcohols to esters and H_2, has a P-da-PNN ligand, a carbonyl trans to the nitrogen in central ring, and a Ru−H bond cis to this nitrogen. A slightly less stable isomer of **1**, **1′** (ΔG_{solv} = 6.6 kcal/mol, ΔH_{gas} = 6.8 kcal/mol), with a N-da-PNN ligand was predicted by the calculation. The optimized structures of **1** and **1′** are shown in Figure 2. Although **1** and **1′** are close in relative energies, the direct conversion between them is not easy because of the activation of C−H bonds for the transfer of a H from one arm to the other arm of the PNN ligand. The importance of **1′** as the actual catalyst in this photolytic cycle and the conversion between **1** and **1′** will be described below with detailed energy barriers.

Table 2. Comparison of Selected Bond Distances (in Å) and Angles (in deg) of **3′** in TPSS Optimized Structure and Experimentally Observed Crystal Structure

bond length	calc.	expt.[2]	bond angle	calc.	expt.[2]
Ru−H1	1.633	1.54	N1−Ru−C1	175.96	173.02
Ru−P	2.274	2.265	N2−Ru−P	160.42	159.12
Ru−N1	2.101	2.097	H1−Ru−O2	167.51	171.9
Ru−N2	2.266	2.241	N1−Ru−O2	84.02	86.94
Ru−C1	1.849	1.820	N2−Ru−O2	80.04	82.44
Ru−O2	2.170	2.261	Ru−O2−H2	110.55	103

Thermal H_2 Evolution. The mechanism for the splitting of the first water molecule and for the formation and release of H_2 in this Ru system is shown in Scheme 2. The solvent-corrected free energy profile for Scheme 2 is shown in Figure 3. Optimized intermediate and transition-state structures in these reactions are shown in Figures 4−7. Unless otherwise noted, the energies mentioned in the text are free energies with solvent corrections.

Initially, the open position trans to the hydride in **1** binds a water molecule and forms intermediate **2** with a Ru−O distance of 2.369 Å ($\Delta G°_{solv}$ = 9.9 kcal/mol, $\Delta H°_{gas}$ = −8.0 kcal/mol). Next, an O−H bond in this H_2O is split easily with the assistance of the unsaturated carbon atom through a very low-barrier transition state $\mathbf{TS_{2,3}}$, which is only 3 kcal/mol higher than **2**, for the formation of a more stable intermediate **3**. Formally,

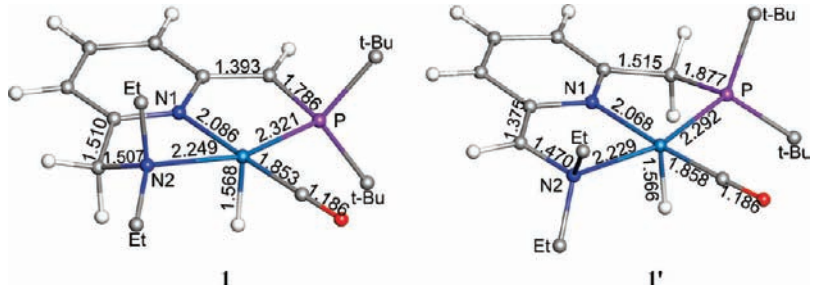

Figure 2. Optimized structures of **1** and **1′**. Bond lengths are in angstroms. Ethyl and *tert*-butyl groups used in DFT calculations are not shown for clarity.

Scheme 2. Mechanism for H_2O Splitting and H_2 Formation and Release

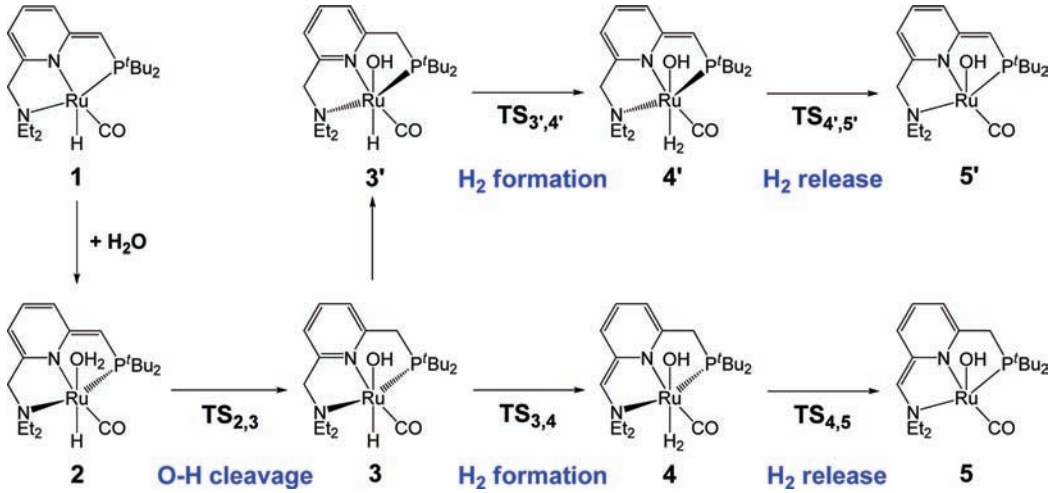

the cleavage of this O−H bond transfers a proton to the unsaturated carbon and results in the aromatization of the central ring of the PNN ligand. The calculated Mulliken charge of the transferring proton in $\mathbf{TS}_{2,3}$ is 0.310. Next, the two five-membered chelate rings can easily twist converting **3** into **3′**, the more stable and experimentally crystallized isomer (Figure 4, $\Delta G^\circ = -2.5$ kcal/mol). In previously reported experimental studies, a similar proton transfer process in **1** has also been invoked in the description of the dehydrogenative coupling of primary alcohols to esters and amines to amides,[5] and such unusual reaction cycles with the ligand dearomatization−aromatization were considered as key steps for metal−ligand cooperation in C−H and H_2 activation by an electron-rich PNP Ir(I) system.[6]

The optimized structure of **3′** using the TPSS functional is compared to its X-ray crystal structure[2] in Table 2. For the selected bond lengths, the differences between calculated and experimental values are less than 0.03 Å except for Ru−H1 and Ru−O2 distances, which have differences of almost 0.1 Å. For the selected bond angles, the differences between calculated and experimental values are less than 4° except for the Ru−O2−H2 angle, which differs by more than 7°. The shorter experimental Ru−H1 distance is typical of the error in X-ray crystal structure measurements of heavy metal−hydrogen bonds. Because the structure of **3′** was optimized in the gas phase, we believe the errors Ru−O2 distance and Ru−O2−H2 angle are due in part to the neglect of the H-bonding interactions between H1/O2 and the water molecules in the observed crystal structure of **3′**. In support of this view, the Ru−O2 distance in $\mathbf{TS}_{2,3}$, where a additional proton is interacting with O2, is 2.273 Å, very close to the experimental value of 2.261 Å in **3′**.

Beginning from **3′**, H_2 is formed by the transfer of a proton from the methylene group at the phosphorus arm of the PNN ligand to the existing Ru−H bond to form the somewhat unstable Ru···H_2 complex **4′** through transition state $\mathbf{TS}_{3',4'}$ (Figure 5) with a solvent-corrected free energy barrier of 32.8 kcal/mol. The Mulliken charges of Ru, the hydride bonding with Ru, and the transferring proton in $\mathbf{TS}_{3',4'}$ are 0.396, −0.475, and 0.101, respectively. With the formation of H_2, the carbon atom bonding to the phosphorus becomes unsaturated again. Next, H_2 is released through transition state $\mathbf{TS}_{4',5'}$ (Figure 5), which is 19.0 kcal/mol higher than **4′** and 34.7 kcal/mol above **1** (+

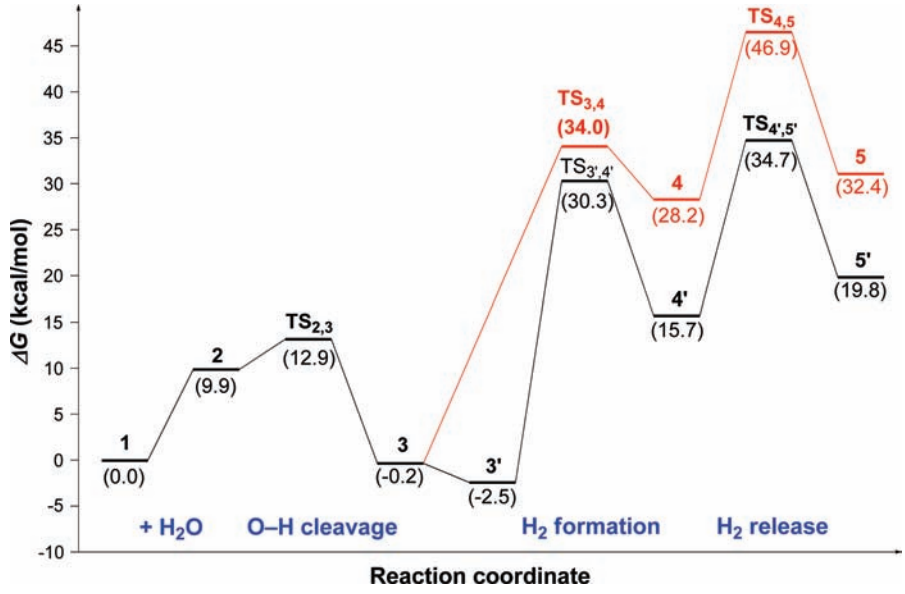

Figure 3. Solvent-corrected free energy profile for the splitting of the first water molecule and the formation and release of H_2.

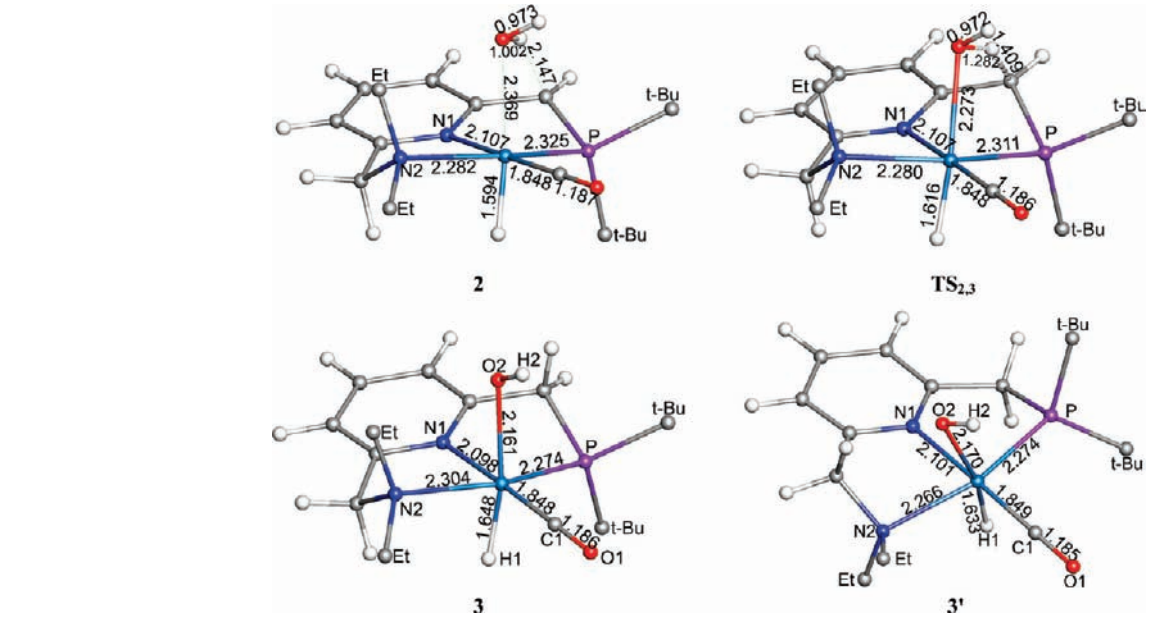

Figure 4. Optimized structures of **2**, **3**, **3′**, and $\mathbf{TS}_{2,3}$ (1297i cm^{-1}) in the splitting of first H_2O. Bond lengths are in angstroms. Ethyl and *tert*-butyl groups used in DFT calculations are not shown for clarity.

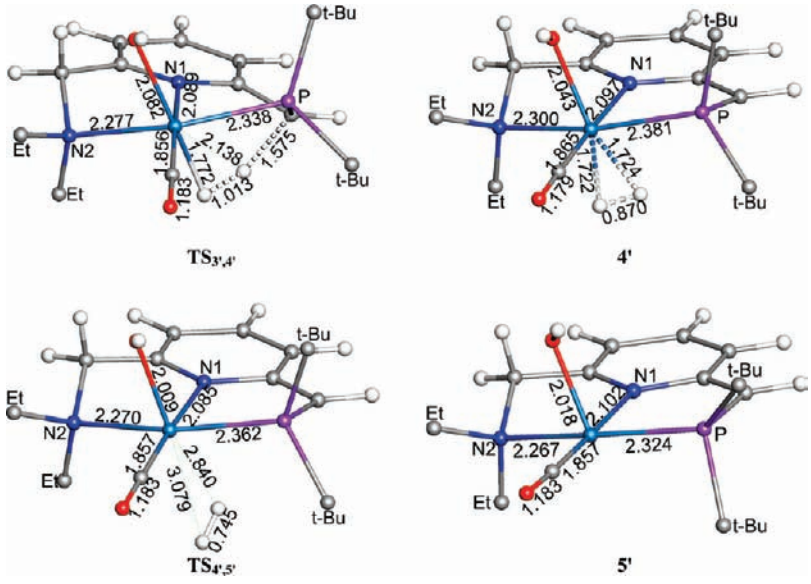

Figure 5. Optimized structures of **4′**, **5′**, $\mathbf{TS}_{3',4'}$ (1232i cm^{-1}), and $\mathbf{TS}_{4',5'}$ (219i cm^{-1}) for H_2 formation and release involving the methylene group at the phosphorus side arm of the PNN ligand. Bond lengths are in angstroms. Ethyl and *tert*-butyl groups used in DFT calculations are not shown for clarity.

H_2O). This high energy barrier for H_2 release is likely overestimated because the calculations do not account for the entropy gain by the dissociating H_2 until it is fully dissociated in **5′**. $\mathbf{TS}_{4',5'}$ also has several kcal/mol more positive solvent free energy correction than **4′** (see the Supporting Information for more details).

Besides the proton transfer from the methylene group on the phosphorus side, described above, a proton could transfer from the methylene group at the nitrogen side arm of the PNN ligand to the hydride bonding with Ru in **3** through $\mathbf{TS}_{3,4}$ (Figure 6), forming the less stable **4**. Next, the H_2 would be released through $\mathbf{TS}_{4,5}$ (Figure 6). Our calculations predict $\mathbf{TS}_{3,4}$ and $\mathbf{TS}_{4,5}$ are 3.7 and 12.2 kcal/mol higher than $\mathbf{TS}_{3',4'}$ and $\mathbf{TS}_{4',5'}$, respectively. Therefore, the methylene group at the nitrogen side arm is unlikely to participate in the formation and release of H_2.

In addition to the above direct methylene proton transfer, another possible route involves electrophilic attack of a water molecule on the hydride ligand of **3′**, which would form **3′-H_2O**, with a dihydrogen bond between the hydride and H_2O.[3] Relative to **3′**, **3′-H_2O** is 10.9 kcal/mol higher in solvent-corrected free energy, but 5.4 kcal/mol lower in gas-phase enthalpy. This 16.3 kcal/mol difference in ΔG and ΔH is mainly the entropy penalty and strong solvation free energy of a water

(4) (a) Zhang, J.; Leitus, G.; Ben-David, Y.; Milstein, D. *J. Am. Chem. Soc.* **2005**, *127*, 10840. (b) Zhang, J.; Gandelman, M.; Shimon, L. J. W.; Milstein, D. *Dalton Trans.* **2007**, 107.
(5) (a) Gunanathan, C.; Ben-David, Y.; Milstein, D. *Science* **2007**, *317*, 790. (b) Zhang, J.; Leitus, G.; Ben-David, Y.; Milstein, D. *Angew. Chem., Int. Ed.* **2006**, *45*, 1113.
(6) Ben-Ari, E.; Leitus, G.; Shimon, L. J. W.; Milstein, D. *J. Am. Chem. Soc.* **2006**, *128*, 15390.

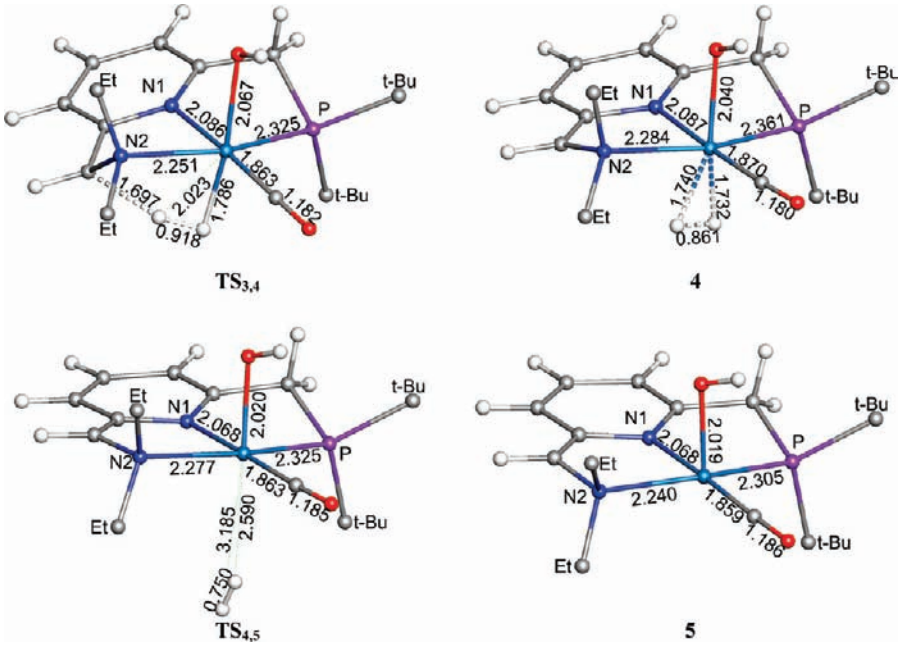

Figure 6. Optimized structures of **4**, **5**, $\mathbf{TS_{3,4}}$ (727i cm^{-1}), and $\mathbf{TS_{4,5}}$ (183i cm^{-1}) for H_2 formation and release involving the methylene group at the nitrogen side arm of the PNN ligand. Bond lengths are in angstroms. Ethyl and *tert*-butyl groups used in DFT calculations are not shown for clarity.

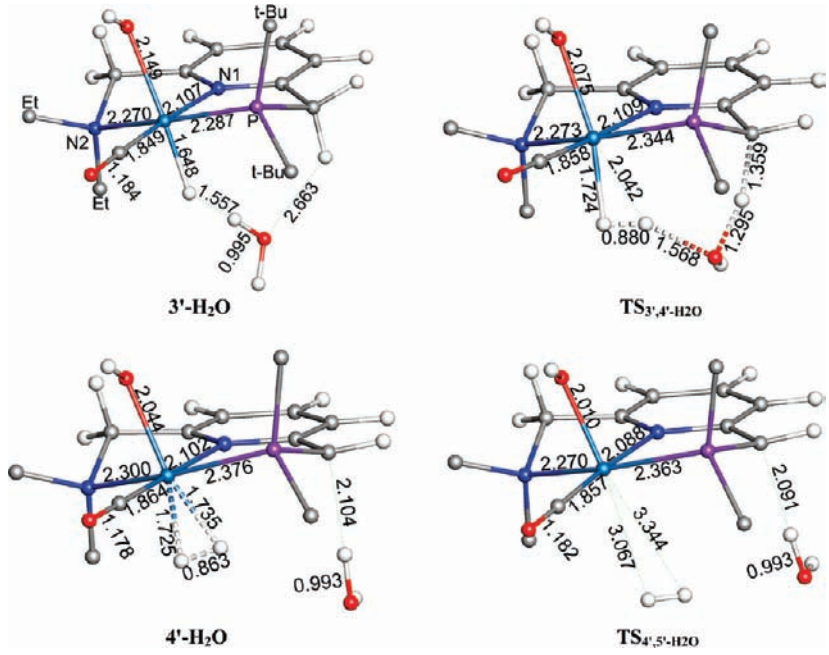

Figure 7. Optimized structures of $\mathbf{3'\text{-}H_2O}$, $\mathbf{4'\text{-}H_2O}$, $\mathbf{TS_{3',4'\text{-}H2O}}$ (1247i cm^{-1}), and $\mathbf{TS_{4',5'\text{-}H2O}}$ (193i cm^{-1}) in H_2 formation and release reactions involving electrophilic attack of a water molecule on the hydride ligand as a bridge for proton transfer from the phosphorus side methylene group. Bond lengths are in angstroms. Ethyl and *tert*-butyl groups used in DFT calculations are not shown for clarity.

molecule in the calculations. In $\mathbf{TS_{3',4'\text{-}H2O}}$, the transition state for the formation of H_2 in this route, the water molecule attached to the hydride ligand acts as a transporter, which captures a proton from methylene and transfers one of its own proton to the hydride bonding with Ru. $\mathbf{TS_{3',4'\text{-}H2O}}$ is 29.1 and 27.3 kcal/mol higher than $\mathbf{3'\text{-}H_2O}$ in solvent-corrected free energy and gas-phase enthalpy, respectively. With the formation of H_2, this water molecule moves to the unsaturated carbon atom and forms $\mathbf{4'\text{-}H_2O}$ with a weak C−H bond. Next, for $\mathbf{4'\text{-}H_2O}$ either the H_2 molecule will be released to form $\mathbf{5'\text{-}H_2O}$ or the H_2O molecule will be released to form **4′**, or both H_2O and H_2 will be released for the formation of **5′**. The optimized structures in this water electrophilic attack route are shown in Figure 7. The energy profile for this reaction pathway is compared to the H_2O free pathway in Figure 8.

Furthermore, because of the weak binding between H_2 and the Ru center (Ru···H_2 distance is about 3 Å), the DFT results of the relative energies of $\mathbf{TS_{4,5}}$, $\mathbf{TS_{4',5'}}$, and $\mathbf{TS_{4',5'\text{-}H2O}}$ are not as reliable as the results of other transition states. Different density functionals give more than 8 kcal/mol difference in energy barrier of $\mathbf{TS_{4',5'}}$ (see section below for the evaluation of density functionals). Further, as mentioned above, standard techniques do not correctly account for the entropy gained by the H_2 in $\mathbf{TS_{4,5}}$, $\mathbf{TS_{4',5'}}$, and $\mathbf{TS_{4',5'\text{-}H2O}}$. A correction for the

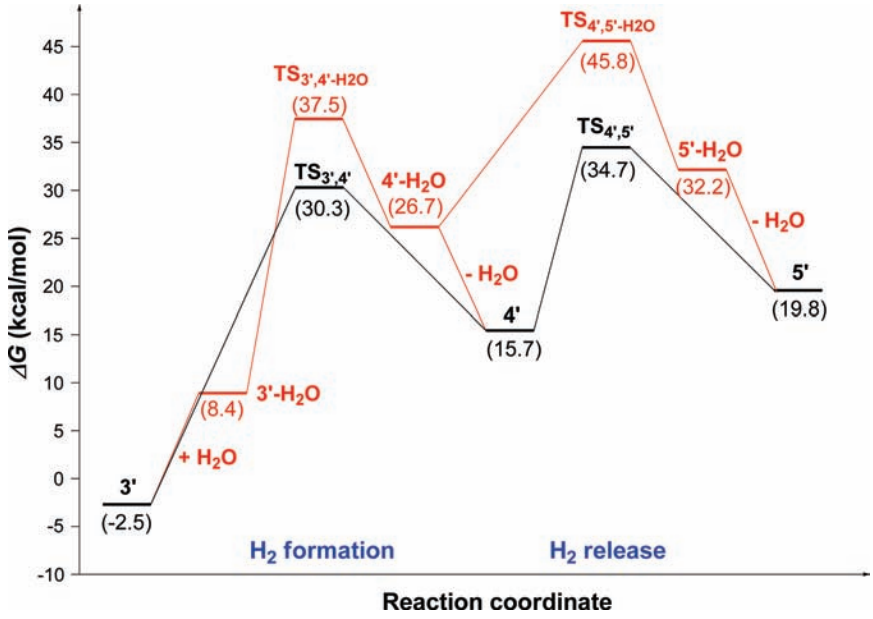

Figure 8. Solvent-corrected free energy profile for the formation of H_2 involving electrophilic attack of a water molecule as a bridge for proton transfer.

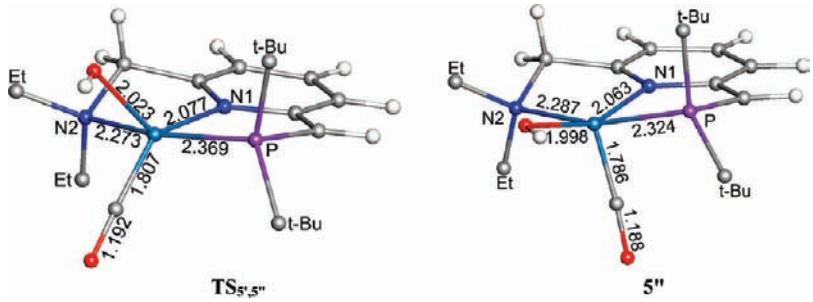

Figure 9. Optimized structures of $\mathbf{TS}_{5',5''}$ (101i cm^{-1}) and **5″**. Bond lengths are in angstroms. Ethyl and *tert*-butyl groups used in DFT calculations are not shown for clarity.

entropy gain could lower these barriers. Therefore, the rate-determining step in this reaction is more likely to be the proton transfer transition state $\mathbf{TS}_{3',4'}$ or $\mathbf{TS}_{3',4'\text{-H2O}}$ for H_2 formation, rather than $\mathbf{TS}_{4',5'}$ as shown in Figure 5. Such large energy barriers of $\mathbf{TS}_{3',4'}$ or $\mathbf{TS}_{3',4'\text{-H2O}}$ explain the observed very slow release rate of H_2 from **3′** (refluxing 100 °C water for 3 days). Here again, the standard free energy and solvation corrections most likely lead to an overestimation of the relative barrier of $\mathbf{TS}_{3',4'\text{-H2O}}$ as compared to $\mathbf{TS}_{3',4'}$. Thus, the direct proton transfer route and the water-assisted route may be competitive.

After H_2 release, because **5′** is not the most stable geometric isomer of this five-coordinate Ru complex, the hydroxyl and carbonyl groups rotate about the N−Ru−P axis through a low-barrier transition state $\mathbf{TS}_{5',5''}$ (9.6 kcal/mol higher than **5′** in free energy, Figure 9), in which CO moves toward the vacant site and OH moves trans to the nitrogen of pyridine, to form **5″**, which is 3.8 kcal/mol more stable than **5′**. From **5′** to **5″**, the Ru−P distance is the same, the Ru−N2 distance increases by 0.02 Å, but the Ru−C, Ru−N1, and Ru−O bond lengths decrease by 0.07, 0.04, and 0.02 Å, respectively. These results indicate that the stronger interaction between Ru and the carbonyl group is the main reason why **5″** is slightly more stable than **5′**. Now the vacant position trans to CO in **5″** is ready to bind another water molecule for further reaction.

Cleavage of the Second Water Molecule. Once the second water molecule attaches to the vacant position in **5″**, its O−H bond is again split rapidly with the assistance of the unsaturated carbon atom (Scheme 3). As shown in Figures 10 and 11, the transition state $\mathbf{TS}_{6,7}$ for the O−H bond cleavage and proton transfer is only 2.3 kcal/mol higher than **6**. Because of the aromatization of the central ring, complex **7** is 13.8 kcal/mol more stable than **6** (like the **2** → **3** transformation) and has been observed experimentally.[2] An alternative reaction pathway for O−H bond cleavage begins with the direct attachment of a water

Scheme 3. Mechanism for the Cleavage of the O−H Bond of the Second Water Molecule

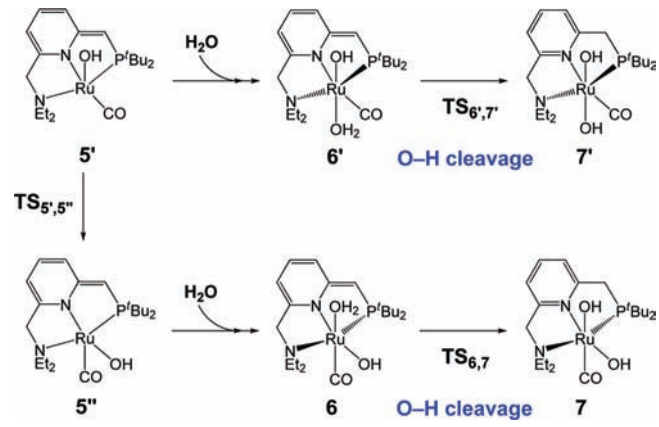

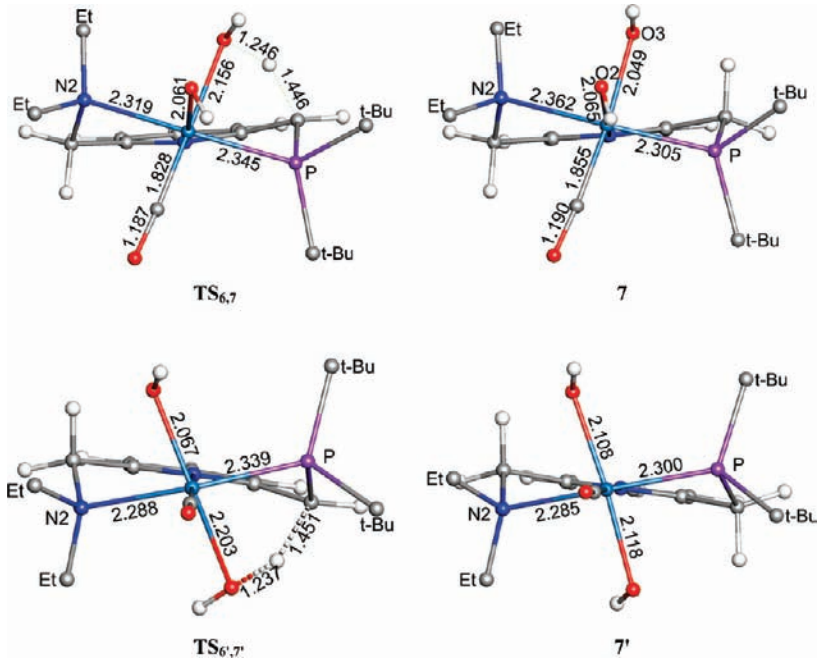

Figure 10. Optimized structures of **7**, **7′**, $\mathbf{TS}_{6,7}$ (1275i cm^{-1}), and $\mathbf{TS}_{6',7'}$ (1192i cm^{-1}). Bond lengths are in angstroms. Ethyl and *tert*-butyl groups used in DFT calculations are not shown for clarity.

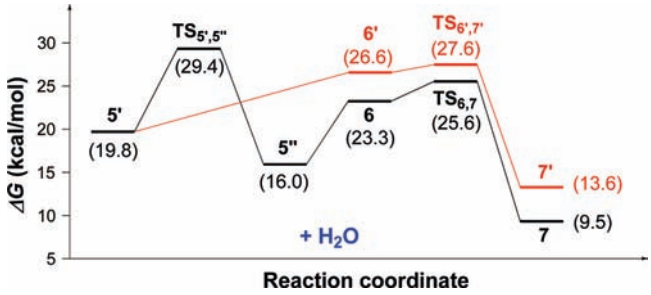

Figure 11. Solvent-corrected free energy profile for the splitting of the second water molecule.

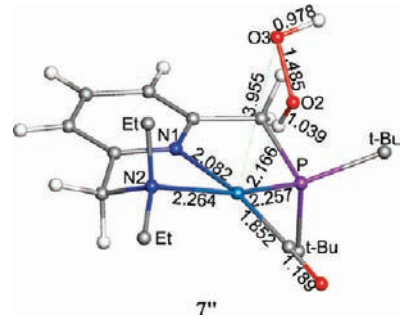

Figure 12. Optimized structures of **7″**. Bond lengths are in angstroms. Ethyl and *tert*-butyl groups used in DFT calculations are not shown for clarity.

molecule to the vacant position trans to the OH group in **5′** forming the unstable intermediate **6′**, which is 3.3 kcal/mol higher than **6** in free energy. Next, $\mathbf{TS}_{6',7'}$ splits the O−H bond of H_2O and transfers a proton to the unsaturated carbon atom forming **7′**, which is 4.1 kcal/mol higher than **7** in free energy. Whereas the two cis OH groups bonding with Ru in **7** are positioned for light-induced, intramolecular, reductive elimination of H_2O_2, which is believed to be the source of O_2 evolution,[2] the two trans OH groups in **7′** cannot easily undergo photolytic reductive elimination to form H_2O_2 directly. However, the barriers back from **7′** to **6′** and **5′** are lower than those from **7** to **6**, which means that even if some **7′** formed, it will eventually be converted to **7**.

TD-DFT Study of the Photolytic Process. Experimentally, when **7** was irradiated with a 300 W halogen lamp, O_2 was formed intramolecularly (confirmed by isotopic labeling). Formation of O_2 is believed to proceed by reductive elimination of H_2O_2 and then disproportionation to O_2 and water. Here, intermediate **7″** (Figure 12), an isomer of **7** with a completely formed H_2O_2 molecule binding to Ru through a weak Ru···H interaction, is calculated as the initial product of photolysis. This **7″** species is 84.4, 81.0, and 82.2 kcal/mol higher than **7** in gas-phase enthalpy, gas-phase free energy, and solvent-corrected free energy, respectively.

The dissociation of H_2O_2 from **7″** produces complex **8** or its isomer **8′** (Figure 13), which is only 1.4 kcal/mol higher than **8**. The gas-phase enthalpy, gas-phase free energy, and solvent-corrected free energy needed for the formation of **8** (**7** → **8** + H_2O_2) are 91.7, 77.2, and 68.6 kcal/mol (311.8, 370.4, and 416.7 nm), respectively, which are consistent with an experimental wavelength of 320−420 nm.

Because of the complexity of this process with the formation of an O−O bond and the breaking of two Ru−O bonds, we have been unable to locate a thermal transition state for the reaction from **7** to **7″**. To examine the key factors in the light-induced intramolecular H_2O_2 formation process, the excited states of **7** and **7″** are calculated first by using the TD-DFT method (see below for computational details). The calculated 10 low-lying excited states and several other higher excited states with stronger oscillator strength (>0.01) of **7** and **7″** are listed in Table 3. For the fully optimized structure of **7**, the calculated transitions at (457.2), (406.1, 367.8, 358.5), and (301.8) nm with strong oscillation strength match well with the observed strong absorption peaks of **7** at 459.3, 379.8, and 297.3 nm. The lowest unoccupied molecular orbital, a pyridine π^* orbital, (LUMO, 114), and the highest occupied molecular orbitals, Ru-based orbitals, (HOMO, 113), (HOMO−1, 112),

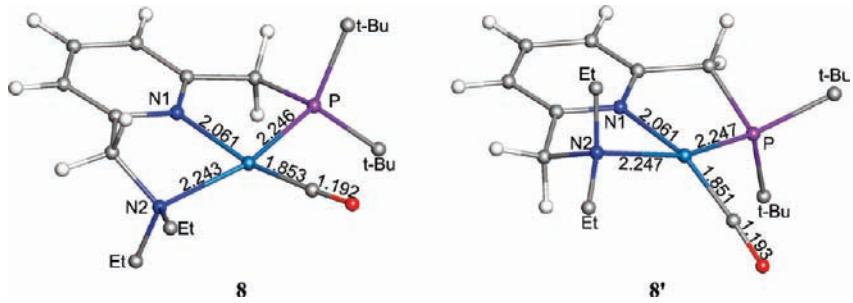

Figure 13. Optimized structures of **8** and **8′**. Bond lengths are in angstroms. Ethyl and *tert*-butyl groups used in DFT calculations are not shown for clarity.

Table 3. TD-DFT Calculated Singlet Excited-State Energies of **7** and **7″** [a]

structure	excited state	primary molecular orbitals	excited energy (eV)	excited wavelength (nm)	oscillator strength
7	1	113 → 114	2.0270	611.65	0.0219
	2	112 → 114	2.1981	564.06	0.0168
	3	113 → 115	2.2837	542.90	0.0059
	4	112 → 115	2.5740	481.68	0.0005
	5	111 → 114	2.7117	457.23	0.0607
	6	111 → 115	2.9692	417.57	0.0007
	7	113 → 116	3.0530	406.11	0.0217
	8	113 → 117	3.2278	384.11	0.0065
	9	112 → 116	3.3710	367.79	0.0115
	10	113 → 118	3.4551	358.84	0.0034
	11	110 → 114	3.4581	358.53	0.0107
	28	113 → 125	4.1081	301.80	0.0135
7″	1	113 → 114	0.8650	1433.35	0.0037
	2	112 → 114	1.3285	933.29	0.0017
	3	113 → 115	1.3752	901.55	0.0005
	4	112 → 115	1.8709	662.70	0.0003
	5	111 → 114	2.1538	575.65	0.0568
	6	113 → 116	2.3095	536.84	0.0054
	7	111 → 115	2.3837	520.14	0.0016
	8	110 → 114	2.4714	501.68	0.0800
	9	113 → 117	2.5322	489.64	0.0115
	10	113 → 118	2.6467	468.45	0.0025
	11	113 → 119	2.7070	458.01	0.0154
	13	113 → 120	2.8576	433.88	0.0372
	15	112 → 117	3.0019	413.02	0.0193
	30	112 → 122	3.5445	349.79	0.0141

[a] HOMO and LUMO are orbitals 113 and 114.

and (HOMO−2, 111) of **7**, are shown in Figure 14. It is clear from Table 3 that the leading transitions are associated with metal to ligand charge transfers involving these orbitals. The large basis set, full-ligand calculations with 50 excited states reported here reproduce the experimental UV−vis spectral values better than the previously reported TD-DFT calculations on a smaller model.[2] In **7″**, H_2O_2 is far away from the metal center and only has weak interaction between Ru and the hydrogen on O2 with a Ru···H distance of 2.166 Å. Transformation from **7** to **7″** not only involves the movement of the two OH groups together form H_2O_2 and the breaking of two Ru−O bonds, but also the CO group rotates about the Ru−P bond to the position trans to the nitrogen atom in the pyridine ring. Because the formation and dissociation of H_2O_2 leaves empty low-lying orbitals on Ru, the first singlet excited state of **7″** is only 0.865 eV higher than its ground singlet state.

To further understand the photolytic process in **7**, we built three structures along the reaction coordinate from **7** to **7″** by fixing O−O, Ru−O2, and Ru−O3 bond lengths at the 25%, 50%, and 75% along the coordinate. Next, with fixed O−O, Ru−O2, and Ru−O3 bond lengths at each structure, all other geometric parameters were optimized to the lowest

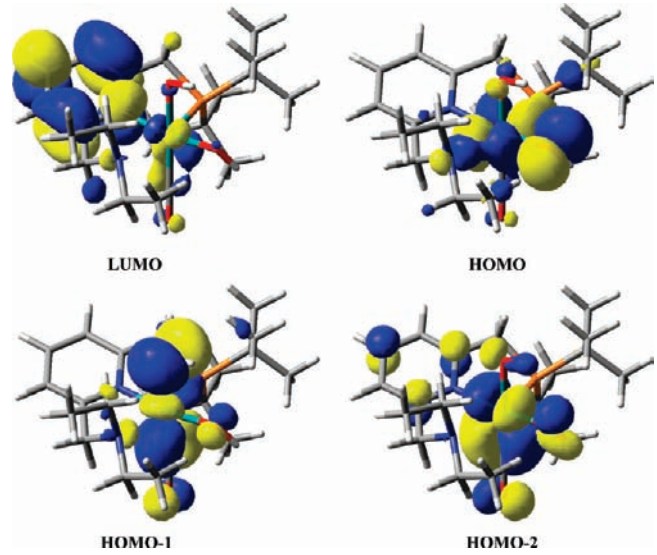

Figure 14. Contour diagrams of DFT calculated LUMO (114), HOMO (113), HOMO−1 (112), and HOMO−2 (111) of **7**.

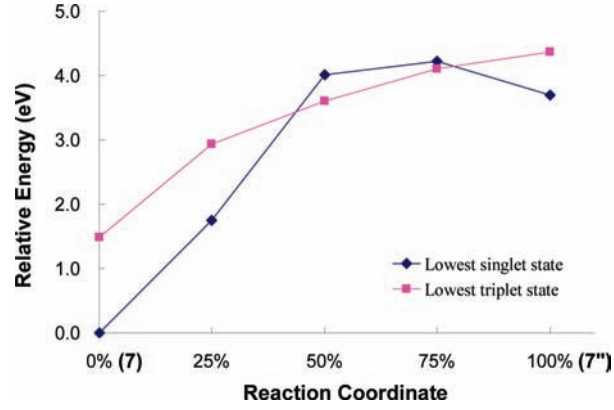

Figure 15. Gas-phase electronic energies of optimized single and triplet state structures along the reaction coordinates from **7** to **7″**.

singlet and triplet states separately. The relative electronic energies of these optimized structures are shown in Figure 15 (see the Supporting Information for detailed structures and relative energies). For **7**, its triplet state was also fully optimized and is about 1.5 eV higher than its singlet ground state. However, the energy of the singlet state of **7** increases more rapidly than that of the triplet state along the reaction coordinate toward **7″**. For the structures close to 50% of the reaction coordinate, the triplet state is already 0.4 eV lower than the singlet state. Next, after the formation of H_2O_2, the triplet state of **7″** again is higher than its singlet state. Thus,

Scheme 4. Mechanism for the Regeneration of **1** and **3′** after Light-Induced O_2 Evolution

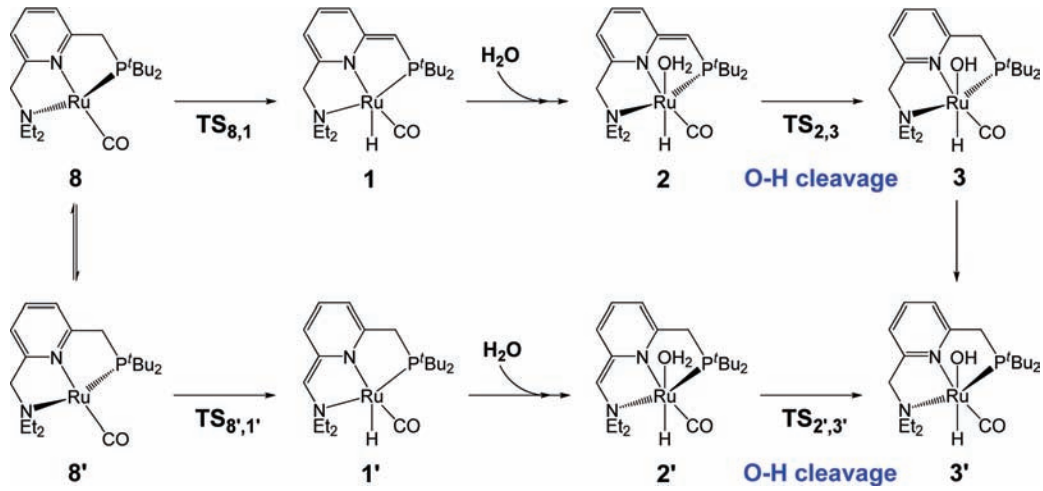

this photolytic reaction may involve two singlet−triplet crossings.[7] After adsorbing a photon, the singlet state decays to a dissociative triplet state, which eventually passes through the high barrier of the singlet state on its path to the dissociation of H_2O_2, eventually decaying to the singlet state in the product. However, as we mentioned above, the DFT results are not sufficiently accurate to actually determine the exact energy of the dissociating state. Furthermore, the high level ab initio calculations are impossible for such large molecular systems.

Regeneration of Complexes 1 and 3′. The mechanism for the regeneration of **1** and **3′** after light-induced H_2O_2 evolution is shown in Scheme 4. The structures of the optimized intermediates and transition states are shown in Figure 16. The corresponding solvent-corrected free energy profile is shown in Figure 17. Beginning with **8**, a H can be transferred from the methylene group at the phosphine side arm of the PNN ligand to the Ru center through transition state $\mathbf{TS_{8,1}}$ (Figure 16), which is 32.1 kcal/mol higher than **8** in solvent-corrected free energy, for regeneration of the initial complex **1**. The Mulliken charge of this H in $\mathbf{TS_{8,1}}$ is −0.624, a value that suggests that the transferring H is quite hydridic in this transition state. With the regeneration of **1**, a potential photocatalytic cycle in agreement with previously proposed mechanism would be obtained. However, instead of the regeneration of **1**, a new lower barrier reaction pathway for the regeneration of **1′** (Figure 2) with a hydride transferred from the methylene group at the nitrogen side arm of the PNN ligand to the Ru center is predicted here.

Species **8** and its slightly less stable isomer, **8′**, easily interconvert. The 1.4 kcal/mol relative free energy difference between **8** and **8′** is mainly steric and caused by the relative position of ethyl and *tert*-butyl groups. Beginning with **8′**, a H can be transferred from the methylene group at the nitrogen side arm of the PNN ligand to the Ru center through transition state $\mathbf{TS_{8',1'}}$ (Figure 16) to form complex **1′**. Although **1′** is 6.6 kcal/mol less stable than **1**, $\mathbf{TS_{8',1'}}$ is 5.3 kcal/mol lower than $\mathbf{TS_{8,1}}$ in free energy. The Mulliken charges of the H transferred to Ru in $\mathbf{TS_{8',1'}}$ and **1′** are −0.439 and −0.486, respectively. Next, a water molecule can attack the vacant position trans to the hydride in **1′** and form the unstable intermediate **2′**. The O−H bond cleavage transition state $\mathbf{TS_{2',3'}}$ appears to be 0.6

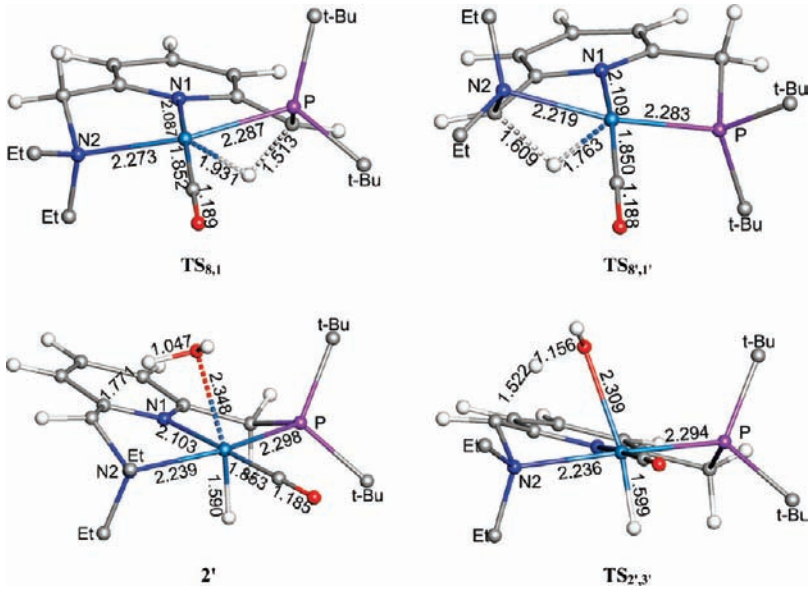

Figure 16. Optimized structures of $\mathbf{TS_{8,1}}$ (1372i cm^{-1}), $\mathbf{TS_{8',1'}}$ (1091i cm^{-1}), **2′**, and $\mathbf{TS_{2',3'}}$ (789i cm^{-1}). Bond lengths are in angstroms. Ethyl and *tert*-butyl groups used in calculations are not shown for clarity.

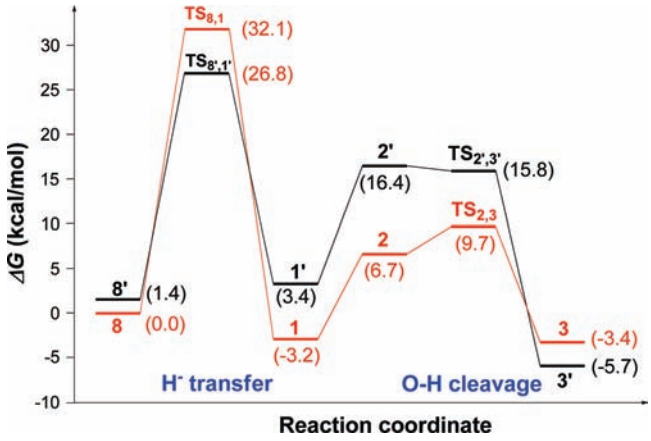

Figure 17. Solvent-corrected free energy profile for the mechanism shown in Scheme 4, the regeneration of **1** and **3′** after light-induced O_2 evolution.

kcal/mol lower than that of **2′**. However, $\mathbf{TS_{2',3'}}$ is 0.4 kcal/mol higher than **2′** in electronic energy; the lower free energy appears to be caused by the use of the harmonic approximation for the vibrational conditions. The Mulliken charge of the proton transferred from H_2O to the unsaturated carbon of N-da-PNN in $\mathbf{TS_{2',3'}}$ is 0.424. Thus, from **8′**, **3′** is regenerated through a lower barrier reaction pathway with the involvement of the methylene group at the nitrogen side arm of the PNN ligand.

Conclusion

On the basis of the experimental study of the Ru-promoted consecutive thermal H_2 and light-induced O_2 evolution from water, Milstein and co-workers proposed a mechanistic framework.[2] Here, the details of the reaction mechanism are developed. Our calculations indicate that the cleavages of the O−H bonds of water molecules are rapid through transfer of protons to the unsaturated carbon atom of the nitrogen or the phosphorus side arm rearomatizing the central ring. Subsequent formation of H_2 by transfer of a methylene proton to the Ru−H bond with the dearomatization of the pyridine appears to be the rate-determining step. TD-DFT calculated excited states of the complex with two cis OH groups reproduced its observed UV−vis absorption spectrum. The photolytic reductive elimination for the breaking of two strong Ru−O bonds and the formation of H_2O_2 occurs from a dissociative triplet state through a singlet−triplet crossing. Instead of the regeneration of initial complex **1** after the light-induced O_2 evolution, a new lower barrier reaction pathway for the regeneration of **3′**, the observed intermediate, involves the methylene group at the nitrogen side arm, rather than the methylene at the phosphors side.

The photocatalytic mechanism reported in this study is unusual in the participation of PNN pincer ligand in the catalytic processes. Ligand modifications may lower the key dearomatization energy barrier, provide a more favorable geometry for methylene H transfer, and increase the overall efficiency for light-driven water splitting into H_2 and O_2. Such unusual participation of unsaturated ligand atoms has also been predicted for the catalytic dehydrogenation of ammonia-borane[8] and H_2 activation by monoiron hydrogenase.[9]

Computational Details

All calculations were performed using the Gaussian 03 suite of ab initio programs[10] at the Tao−Perdew−Staroverov−Scuseria[11] (TPSS) functional with all-electron 6-31++G(d,p) basis set for H, C, N, O, and P atoms and Stuttgart fully relativistic effect core potential (ECP) with augmented correlation consistent polarized valence double *zeta* basis set (ECP28MDF_AVDZ) for Ru.[12] We believe such basis sets (700 basis functions and 1283 primitive Gaussians for **1**) used in our study are sufficient for accurate DFT calculations. The geometric structures of all species were optimized as gas phase. Calculating the harmonic vibrational frequencies and noting the number of imaginary frequencies confirmed the nature of all intermediates (no imaginary frequency) and transition state structures (only one imaginary frequency). The latter were also confirmed to connect reactants and products by intrinsic reaction coordinate (IRC) calculations. The gas-phase free energies, G, were calculated at $T = 298.15$ K within the harmonic potential approximation at optimized structures. The effect of solvent was taken into account by single point calculations on gas-phase optimized structures using integral equation formalism polarizable continuum model (IEFPCM) for water ($\varepsilon = 78.3553$). In TD-DFT calculations, 50 singlet excited states were calculated at optimized structures by using the TPSS functional and the same basis sets mentioned above. The transitions to triplet and higher order multiplet excited states from the ground state are forbidden because the ground states of the species in this study are singlets. Even if some of these forbidden transitions gain intensity by spin−orbit splitting, their intensities in absorption spectrum should still be very weak relative to the transitions to the singlet excited states. Therefore, the detailed effects of spin−orbit coupling do not need to be considered in the calculations for the simulation of absorption spectrum. Because the excited-state structures cannot be optimized by using the TD-DFT method, the lowest triplet states were optimized by specifying the spin state in unrestricted DFT calculations. The 3D molecular structures displayed in this Article were drawn by using the JIMP2 molecular visualizing and manipulating program.[13]

Evaluation of Density Functionals

To examine the effect of different density functionals on the calculated energy barriers in this transition metal system with the same basis sets, nine of the most popular density functionals were selected for evaluation: generalized gradient approximation (GGA) functionals BP86[14] and PBE,[15] meta-GGA functional TPSS,[11] hybrid GGA functionals PBE1PBE,[16] B3LYP,[17] and B3PW91,[18] and hybrid meta-GGA functionals TPSSh,[11] BMK,[19] and M05.[20] The calculated electronic energy barriers of three rate-determining steps, H_2 formation (**3′** → $\mathbf{TS_{3',4'}}$), H_2 release (**4′** → $\mathbf{TS_{4',5'}}$), and the regeneration of catalyst (**8** → $\mathbf{TS_{8,1}}$), at TPSS optimized structures are listed in Table 4. For the proton transfer and hydride transfer transition states $\mathbf{TS_{3',4'}}$ and $\mathbf{TS_{8,1}}$, pure density functionals without Hartree−Fock exchange and hybrid meta-GGA functionals have very close energy barriers, slightly lower than the energy barriers obtained

(7) The crossing of singlet and triplet states was also observed in other potential energy scans that involved the O−Ru−O angle or O−O distance. However, while scanning for smaller O−Ru−O angles or O−O distances, the Ru−OH bonds remained strong even when the O−O distances are smaller than that in free H_2O_2. Thus, the total energy increases drastically with scans that only decrease the O−O distance. Therefore, the scan of potential energy curves with varying only the O−Ru−O angle or the O−O distance cannot reflect the observed photolytic reductive-elimination process from **7**.

(8) (a) Yang, X.; Hall, M. B. *J. Am. Chem. Soc.* **2008**, *130*, 1798. (b) Yang, X.; Hall, M. B. *J. Organomet. Chem.* **2009**, *694*, 2831.
(9) (a) Yang, X.; Hall, M. B. *J. Am. Chem. Soc.* **2008**, *130*, 14036. (b) Yang, X.; Hall, M. B. *J. Am. Chem. Soc.* **2009**, *131*, 10901.
(10) Frisch, M. J. *Gaussian 03*, revision E.01; Gaussian, Inc.: Wallingford, CT, 2004.
(11) Tao, J. M.; Perdew, J. P.; Staroverov, V. N.; Scuseria, G. E. *Phys. Rev. Lett.* **2003**, *91*, 146401.
(12) Peterson, K. A.; Figgen, D.; Dolg, M.; Stoll, H. *J. Chem. Phys.* **2007**, *126*, 124101.

Table 4. Relative Electronic Energies of the Rate-Determining Steps: H_2 Formation (**3′** → $\mathbf{TS_{3',4'}}$), H_2 Release (**4′** → $\mathbf{TS_{4',5'}}$), and the Regeneration of Catalyst (**8** → $\mathbf{TS_{8,1}}$) Obtained from Single-Point Calculations Using Different Density Functionals at TPSS Optimized Structures

density functional	relative electronic energies (kcal/mol)		
	$E^{\ddagger}(\mathbf{TS_{3',4'}}) - E^{\circ}(\mathbf{3'})$	$E^{\ddagger}(\mathbf{TS_{4',5'}}) - E^{\circ}(\mathbf{4'})$	$E^{\ddagger}(\mathbf{TS_{8,1}}) - E^{\circ}(\mathbf{8})$
BP86	33.66	21.81	32.19
PBE	33.23	21.83	31.78
TPSS	33.88	19.65	32.42
PBE1PBE	36.69	21.36	34.31
B3LYP	38.20	16.66	37.07
B3PW91	36.49	20.59	34.73
TPSSh	34.84	19.72	33.60
BMK	34.95	13.49	32.57
M05	36.53	13.26	35.91

from Hybrid GGA functionals, especially for B3LYP, which has the highest barriers in both cases. For the H_2 release transition state, $\mathbf{TS_{4',5'}}$, because of the weak bonding and long distance between H_2 and Ru, the difference in energy barriers obtained from different functionals is larger than 8 kcal/mol. The TPSS energy barrier is in the middle of this range. Because of some arguments about the reliability of B3LYP when it is applied to transition metal complexes in recent years,[21] the TPSS functional was selected for DFT calculations in this study. Generally, TPSS has excellent performance for relative barriers. It is the only meta-GGA level functional without empirical parameters, and it has a much higher computational efficiency than do hybrid functionals.

Acknowledgment. We acknowledge financial support from the NSF (CHE-0518074, CHE-0541587, and DMS-0216275) and The Welch Foundation (A-0648). We appreciate constructive discussion with Dr. Simon W. North (Texas A&M University, College Station, Texas).

Supporting Information Available: Complete ref 10, gas-phase absolute energies, solvent free energy corrections, and atomic coordinates of optimized stationary points and transition states. This material is available free of charge via the Internet at http://pubs.acs.org.

JA9041065

(13) (a) Manson, J.; Webster, C. E.; Hall, M. B. *JIMP2, version 0.091, a free program for visualizing and manipulating molecules*; Texas A&M University: College Station, TX, 2006. (b) Hall, M. B.; Fenske, R. F. *Inorg. Chem.* **1972**, *11*, 768.

(14) (a) Becke, A. D. *Phys. Rev. A* **1988**, *93*, 3098. (b) Perdew, J. P. *Phys. Rev. B* **1986**, *33*, 8822.

(15) (a) Perdew, J. P.; Burke, K.; Ernzerhof, M. *Phys. Rev. Lett.* **1996**, *77*, 3865. (b) Perdew, J. P.; Burke, K.; Ernzerhof, M. *Phys. Rev. Lett.* **1997**, *78*, 1396.

(16) Adamo, C.; Barone, V. *J. Chem. Phys.* **1999**, *110*, 6158.

(17) (a) Becke, A. D. *J. Chem. Phys.* **1993**, *98*, 5648. (b) Lee, C.; Yang, W.; Parr, R. G. *Phys. Rev. B* **1988**, *37*, 785.

(18) (a) Burke, K.; Perdew, J. P.; Wang, Y. In *Electronic Density Functional Theory: Recent Progress and New Directions*; Dobson, J. F., Vignale, G., Das, M. P., Eds.; Plenum: New York, 1998. (b) Perdew, J. P. In *Electronic Structure of Solids '91*; Ziesche, P., Eschrig, H., Eds.; Akademie Verlag: Berlin, 1991. (c) Perdew, J. P.; Chevary, J. A.; Vosko, S. H.; Jackson, K. A.; Pederson, M. R.; Singh, D. J.; Fiolhais, C. *Phys. Rev. B* **1992**, *46*, 6671. (d) Perdew, J. P.; Chevary, J. A.; Vosko, S. H.; Jackson, K. A.; Pederson, M. R.; Singh, D. J.; Fiolhais, C. *Phys. Rev. B* **1993**, *48*, 4978. (e) Perdew, J. P.; Burke, K.; Wang, Y. *Phys. Rev. B* **1996**, *54*, 16533.

(19) Boese, A. D.; Martin, J. M. L. *J. Chem. Phys.* **2004**, *121*, 3405.

(20) Zhao, Y.; Schultz, N. E.; Truhlar, D. G. *J. Chem. Phys.* **2005**, *123*, 161103.

(21) (a) Paier, J.; Marsman, M.; Kresse, G. *J. Chem. Phys.* **2007**, *127*, 024103. (b) Harvey, J. N. *Annu. Rep. Prog. Chem., Sect. C* **2006**, *102*, 203. (c) Sousa, S. F.; Fernandes, P. A.; Ramos, M. J. *J. Phys. Chem. A* **2007**, *111*, 10439. (d) Furche, F.; Perdew, J. P. *J. Chem. Phys.* **2006**, *124*, 044103.